



# Hydrogen incorporation and charge balance in natural zircon

J.C.M. De Hoog<sup>a,\*</sup>, C.J. Lissenberg<sup>b</sup>, R.A. Brooker<sup>c</sup>, R. Hinton<sup>a</sup>, D. Trail<sup>d</sup>,  
E. Hellebrand<sup>e</sup>, EIMF<sup>a</sup>

<sup>a</sup> *Edinburgh Ion Microprobe Facility, School of GeoSciences, University of Edinburgh, West Mains Road, Edinburgh EH9 3JW, United Kingdom*

<sup>b</sup> *School of Earth and Ocean Sciences, Cardiff University, Main Building, Park Place, Cardiff CF10 3AT, United Kingdom*

<sup>c</sup> *School of Earth Sciences, University of Bristol, Wills Memorial Building, Queen's Road, Clifton BS8 1RJ, United Kingdom*

<sup>d</sup> *Department of Earth and Environmental Sciences, Rensselaer Polytechnic Institute, Troy, NY 12180, United States*

<sup>e</sup> *Department of Geology and Geophysics, University of Hawai'i at Mānoa, 1680 East-West Road, Honolulu, HI 96822, United States*

Received 4 January 2014; accepted in revised form 30 June 2014; Available online 15 July 2014

## Abstract

The water and trace element contents of natural igneous zircons were determined to constrain the mechanism of hydrogen incorporation. The low radiation-damage zircons were derived from Fe–Ti oxide gabbros from the Vema Fracture Zone (11°N, Mid-Atlantic Ridge). They contain up to 1212 ppmw H<sub>2</sub>O, 1.9 wt.% Y<sub>2</sub>O<sub>3</sub> and 0.6 wt.% P<sub>2</sub>O<sub>5</sub> and are generally strongly zoned. REE + Y are partially charge-balanced by P (Y, REE<sup>3+</sup> + P<sup>5+</sup> = Zr<sup>4+</sup> + Si<sup>4+</sup>), but a large REE excess is present. On an atomic basis, this excess is closely approximated by the amount of H present in the zircons. We therefore conclude that H is incorporated by a charge-balance mechanism (H<sup>+</sup> + REE<sup>3+</sup> = Zr<sup>4+</sup>). This interpretation is consistent with FTIR data of the Vema zircons, which shows a strongly polarised main absorption band at ca. 3100 cm<sup>-1</sup>, similar to experimentally grown Lu-doped hydrous zircon. The size of this 3100 cm<sup>-1</sup> band scales with H and REE contents. Apart from a small overlapping band at 3200 cm<sup>-1</sup>, no other absorption bands are visible, indicating that a hydrogrossular-type exchange mechanism does not appear to be operating in these zircons. Because of charge-balanced uptake of H, P and REE in zircon, the partitioning of these elements into zircon is dependent on each of their concentrations. For instance,  $D_{\text{zrc/melt}}^{\text{REE}}$  increases with increasing H and P contents of the melt, whereas  $D_{\text{zrc/melt}}^{\text{H}}$  increases with increasing REE content but decreases with increasing P content. In addition, H–P–REE systematics of sector zoning indicate kinetic effects may play an important role. Hence, using H in zircon to determine the water content of melts is problematic, and REE partitioning studies need to take into account P and H<sub>2</sub>O contents of the melt.

Crown copyright © 2014 Published by Elsevier Ltd. This is an open access article under the CC BY license (<http://creativecommons.org/licenses/by/3.0/>).

## 1. INTRODUCTION

The amount of water in nominally anhydrous minerals (NAMs, minerals without water in their structural formulae) has received great interest, as NAMs may hold most of the Earth's water budget, their water content has significant effect on mineral and rock properties such as mechanical strength and electrical conductivity, and play a role in global

geodynamics, such as the location of mantle discontinuities and depth of mantle melting (Smyth, 1987; Jacobsen, 2006; Kohlstedt, 2006; Ohtani and Litasov, 2006; Regenauer-Lieb, 2006). In igneous rocks, the water content of NAMs may be used to reconstruct magma water contents (e.g., Kohn and Grant, 2006). The mechanism by which water (or hydroxyl) is incorporated in minerals is essential for understanding and evaluating these processes. Water uptake is often related to vacancy substitution, i.e., crystal defects (Smyth, 2006), but incorporation of other trace elements can play an essential role (e.g., Berry et al., 2005).

\* Corresponding author. Tel.: +44 31 650 8525.

E-mail address: [ceesjan.dehoog@ed.ac.uk](mailto:ceesjan.dehoog@ed.ac.uk) (J.C.M. De Hoog).

Zircon is a common accessory mineral and one of the most versatile geological tools, with applications ranging from U–Pb dating of igneous, metamorphic rocks and sediments, trace element contents to determine rock paragenesis and evolution, whereas oxygen, hafnium and lithium isotope studies can provide information about the genetic environment of ancient rocks (e.g., [Wilde et al., 2001](#); [Cavosie et al., 2005, 2011](#); [Trail et al., 2007](#); [Harrison et al., 2008](#); [Ushikubo et al., 2008](#)). In addition, trace elements such as REE can be used to determine the oxidation state of magmas, whereas Ti-thermometry may provide information about zircon crystallisation temperature ([Ferry and Watson, 2007](#); [Trail et al., 2007, 2012](#); [Grimes et al., 2009](#); [Burnham and Berry, 2012](#)).

In contrast, the water content of zircon has received relatively little attention, perhaps due to the low abundance of zircon and, as a result, its limited effect on water budgets of Earth's reservoirs, as well as the likelihood of the presence secondary H due to radiation damage of zircons. The limited data so far suggests low water contents of <0.01 wt.% in most natural zircons ([Woodhead et al., 1991b](#); [Bell et al., 2004](#)). Larger amounts of water (up to 16.6%; [Fronzel, 1953](#); [Coleman and Erd, 1961](#)) can be present in metamict zircon, but this is a result of a secondary process related to destruction of the crystal structure by radiation damage due to the presence of radioactive elements such as U and Th ([Aines and Rossman, 1986](#); [Woodhead et al., 1991b](#); [Nasdala et al., 2001](#)). Trace elements may play a dominant role in the uptake of water in zircon, as charge imbalance in zircon (REE exceeding P) is common ([Speer, 1980](#)) and incorporation of Al, Fe, Mg and Li has been proposed to provide charge balance ([Hanchar et al., 2001](#); [Hoskin and Schaltegger, 2003](#)). However, charge balance could also be attained by the presence of hydrogen (e.g., [Woodhead et al., 1991b](#); [Hinton et al., 2003](#); [Trail et al., 2011](#)), but no study exploring this relation for natural zircon yet exists.

Here we present a detailed study of water and trace element contents of natural, non-metamict zircons to constrain the mechanism of water incorporation into zircon, to determine whether water plays a role in maintaining charge balance, and to investigate if water contents of igneous zircons may be used to reconstruct the water content of host magmas.

### 1.1. Sample suite

Zircons were separated from Fe–Ti oxide gabbros from oceanic crust exposed at the Vema Lithospheric Section (VLS) at 11°N on the Mid-Atlantic Ridge ([Auzende et al., 1988](#); [Brunelli et al., 2006](#); [Lissenberg et al., 2009](#)). This suite of zircons is ideally suited for this study as they are primary magmatic zircons from a well-constrained magma source, have young ages (ca. 14 Ma) and have therefore suffered negligible radiation damage  $D\alpha < 10^{18}$   $\alpha$  decay events/g ([Murakami et al., 1991](#)), and show a range of trace element zoning features, such as normal, oscillatory and sector zoning ([Lissenberg et al., 2009](#)).

The VLS is exposed along the southern wall of the transverse ridge of the Vema Fracture Zone, which rises from 5100 to 450 m below sea level. It exposes a full section of

mantle peridotites, lower crustal gabbros and basaltic upper crust formed along the Mid-Atlantic Ridge ([Auzende et al., 1988, 1989](#); [Bonatti et al., 2003, 2005](#)). The studied samples were collected by submersible craft and by dredging along a section of the VLS centred around 42°30'W and ca. 4–5000 m depth ([Table 1](#)). The gabbros commonly contain Fe–Ti oxides, indicating extensive differentiation.

Here we present data from nine zircon grains and grain fragments from four samples ([Table 1](#)). This is a subset of a larger study ([Lissenberg et al., 2009](#); in preparation). Zircons range in size from 75 to 500  $\mu\text{m}$  and generally show a subhedral to euhedral prismatic habit. Many show complex zoning patterns, but do not have xenocrystic cores and appear to have a continuous magmatic growth history. Some zircons show signs of resorption and later overgrowth ([Figs. 1 and 2](#)). These features are discussed in more detail in [Section 3.1](#).

## 2. ANALYTICAL TECHNIQUES

### 2.1. Imaging and chemical maps (EPMA)

X-ray distribution maps were acquired with the JEOL JXA-8500F field-emission electron probe micro-analyzer at the University of Hawaii, using the following analytical conditions: 15 keV accelerating potential, 100 nA probe current and focused beam, 50 ms dwell time per pixel, a step size of 0.5–1.5  $\mu\text{m}$  using a stage with linear encoders, and a resolution of individual maps of 250–550 pixels in X by 350–1000 pixels in Y. The Y-L $\alpha$  distribution maps shown in [Figs. 1 and 2](#) are based on combining the counts collected simultaneously on three or four spectrometers (1 PETH crystal with a Xe-sealed detector, 1 PETH crystal with gasflow detector, 1–2 PETJ with gasflow detector).

### 2.2. Trace elements (SIMS)

Trace elements were measured by ion microprobe (Secondary Ion Mass Spectrometry, SIMS) using a Cameca 4f monocollector instrument at the Edinburgh Ion Microprobe Facility. A beam of  $^{16}\text{O}^-$  was accelerated to 14.5 kV and impacted onto gold-coated samples. Two beam currents were used depending on the size of the area to be analysed: a 10 nA beam resulting in a sputtered area of ca. 20  $\mu\text{m}$  diameter and a 2.5 nA beam resulting in a sputtered area of ca. 10  $\mu\text{m}$ . High energy ( $120 \pm 20$  eV) secondary ions were extracted and accelerated into the mass spectrometer and counted using an electron multiplier. The instrument was operated in low mass resolution mode.

The following isotopes were measured:  $^{30}\text{Si}$ ,  $^{31}\text{P}$ ,  $^{40}\text{Ca}$ ,  $^{49}\text{Ti}$ ,  $^{89}\text{Y}$ ,  $^{138}\text{Ba}$ ,  $^{139}\text{La}$ ,  $^{140}\text{Ce}$ ,  $^{141}\text{Pr}$ ,  $^{143}\text{Nd}$ ,  $^{149}\text{Sm}$ ,  $^{151}\text{Eu}$ ,  $^{157}\text{Gd}$ ,  $^{159}\text{Tb}$ ,  $^{161}\text{Dy}$ ,  $^{165}\text{Ho}$ ,  $^{167}\text{Er}$ ,  $^{169}\text{Tm}$ ,  $^{171}\text{Yb}$ ,  $^{175}\text{Lu}$ ,  $^{178}\text{Hf}$ ,  $^{232}\text{Th}$ ,  $^{238}\text{U}$ . In addition mass 130.5 was measured to determine the electron multiplier background signal and mass 134 ( $^{90}\text{Zr}^{28}\text{Si}^{16}\text{O}$ ) to allow correction of the ZrSiO interferences on Ba, La, Ce and Pr. Each analysis consisted of six cycles (sweeps through the mass spectrum). Counting times ranged from 2 s for major elements to 20 s for the lowest abundance isotopes ( $^{149}\text{Sm}$ ,  $^{151}\text{Eu}$ ) for a total analysis time of 948 s (excluding waiting times while cycling the magnet).

Table 1  
Location and characteristics of gabbro samples from the Vema Lithospheric Section.

Sample	Latitude	Longitude	Depth (mbsl)	Lithology	Zircon description
VE02-05 <sup>a</sup>	10.674°N	42.724°W	Not recorded	Undeformed, medium to coarse grained oxide gabbro	75–500 μm, subhedral to euhedral prismatic, commonly lacking internal structure, minor sector zoning
S1904-03 <sup>b</sup>	10.710–10.692°N	43.033–43.028°W	4900–4500	Strongly deformed, coarse grained oxide gabbro	150–700 μm, subhedral to euhedral prismatic, prominent sector and oscillatory zoning, some grains with apparent core-rim relationships and altered domains
S1923-01 <sup>b</sup>	10.703–10.687°N	42.575–42.594°W	5200–4000	Moderately deformed, coarse grained orthopyroxene-bearing oxide gabbro	60–600 μm, predominantly grain fragments, prominent sector zoning, lesser oscillatory zoning
S1923-36 <sup>b</sup>	10.703–10.687°N	42.575–42.594°W	5200–4000	Strongly deformed, medium to coarse grained orthopyroxene-bearing oxide gabbro	110–350 μm, subhedral to euhedral prismatic, prominent sector and minor oscillatory zoning, some grains lacking internal structure, rare grains with apparent core-rim relationships and altered domains

<sup>a</sup> VE02-05: Vemanaute cruise, RV *Nadir* (Auzende et al., 1988, 1989).

<sup>b</sup> S1904, S1923: Cruise S19, RV *A.N. Strakhov* (Brunelli et al., 2006).

Raw count rates of heavy rare earth elements were corrected for interferences from oxides of lighter isotopes (e.g., <sup>159</sup>Tb<sup>16</sup>O on <sup>175</sup>Lu) based on previously determined oxide production rates for the energy offset used (120 V). Due to the HREE-enriched pattern of zircons these corrections were generally negligible (<0.5%). Signals for <sup>139</sup>La, <sup>140</sup>Ce and <sup>141</sup>Pr were corrected for ZrSiO interference based on measured <sup>90</sup>Zr<sup>28</sup>Si<sup>16</sup>O. This correction is 21% for La, Ce 2% and Pr 5% on zircon 91500.

Calibration was performed using NIST SRM610 using preferred values from Georem (Jochum et al., 2011) and using its SiO<sub>2</sub> content as an internal standard. Zircon 91500 (Wiedenbeck et al., 2004) and SL1 (Maas et al., 1992) were used as secondary standards to monitor accuracy and precision. Most measured REE values for zircon 91500 are slightly lower than values from Wiedenbeck et al. (2004), which is typical for SIMS data, but are within 15% except for Yb (–22%). Rather large discrepancies are observed for Pr and La, which are 2 and 10 times too high, respectively. Both elements have very low concentrations (0.006 and 0.024 ppmw, respectively) and hence count rates are (<0.5 cps) are sensitive to, e.g., detector noise, but Nd and Sm have similar low count rates and do not show poor accuracy. Additional interferences could be ZrSiOH on La, Zr(OH)<sub>3</sub> on Pr and Nd, and CeH on Pr, but these are difficult to quantify. As Pr and La have lowest concentrations, they are most sensitive to surface contamination. Note that these elements are negligible for the total REE content of zircon. Measured Y + REE in zircon 91500 is identical to the reference value (282 ± 6 ppmw). 1σ uncertainties based on 18 repeat analysis of zircon 91500 throughout the analytical session are 2% for Y, 4–6% for REE > 2 ppmw, 10–20% for REE between 0.5–2 ppmw and 20–60% for REE < 0.2 ppmw.

### 2.3. Water analysis (SIMS)

Water and selected trace elements were measured in the ion probe pits of previous trace element analyses described above, as well as in new locations in a more detailed study of one grain (S1904-03\_XL5) after remounting in indium.

No significant differences were observed between H<sub>2</sub>O measurement in new or old pits on standard materials. The same Cameca 4f instrument was used, using a <sup>16</sup>O<sup>–</sup> beam of 3 nA in low resolution mode. An energy window of 75 ± 20 V was used for secondary ions.

The following isotopes were measured: <sup>1</sup>H, <sup>7</sup>Li, <sup>30</sup>Si, <sup>31</sup>P, <sup>40</sup>Ca, <sup>89</sup>Y. A small subset of zircons was measured for additional trace elements (<sup>19</sup>F, <sup>26</sup>Mg, <sup>27</sup>Al, <sup>54</sup>Fe, <sup>94</sup>ZrH and <sup>93</sup>Nb (corrected for <sup>92</sup>ZrH)), but these elements were present in negligible amounts compared to REE and therefore not measured for all zircons. Each analysis consisted of ten cycles with counting times of 2 s for Si, 3 s for Ca and 5 s for all other isotopes. Phosphorus and Y were measured to allow comparison with trace element data obtained on the same analytical spots as well as to get simultaneous H, P and Y data which is important for charge-balance investigations (Sections 3 and 4). Note that even though REE are not measured during this run, previous trace element analyses on the same spots (Section 2.2) indicated an excellent correlation between Y<sub>2</sub>O<sub>3</sub> and REE<sub>2</sub>O<sub>3</sub> contents ( $r^2 = 0.995$ ; Fig. 3). Therefore, Y + REE contents can be calculated from Y contents with a minimum of uncertainty.

Due to the low water content of zircons it is imperative to minimise water background signals. This was achieved in several ways: (1) samples were held for at least 48 h prior to analysis under high vacuum conditions (<10<sup>–7</sup> mbar in airlock, <5 × 10<sup>–9</sup> mbar in sample chamber); (2) analysis spots were pre-sputtered for 3 min while rastering the beam over an area ca. 20 μm wider than the analysis spot; (3) a narrow field aperture was used so that only ions from the inner 8 μm of the analysis spot are collected in the mass spectrometer; (4) only the last 5 cycles of each analysis are used to integrate the H signal (signals tend to drop about 20–40% during the first 3–4 cycles but are constant after that); (5) use of liquid N<sub>2</sub> cold finger in the sample chamber, as well as a cryogenic pump operating at 16 K; (6) whilst initial analyses were performed on zircons mounted in epoxy, grain S1904-03\_XL5 used for the detailed study was remounted in indium.

The strategy detailed above resulted in relatively constant backgrounds of H<sup>+</sup> of 18–21 counts per second

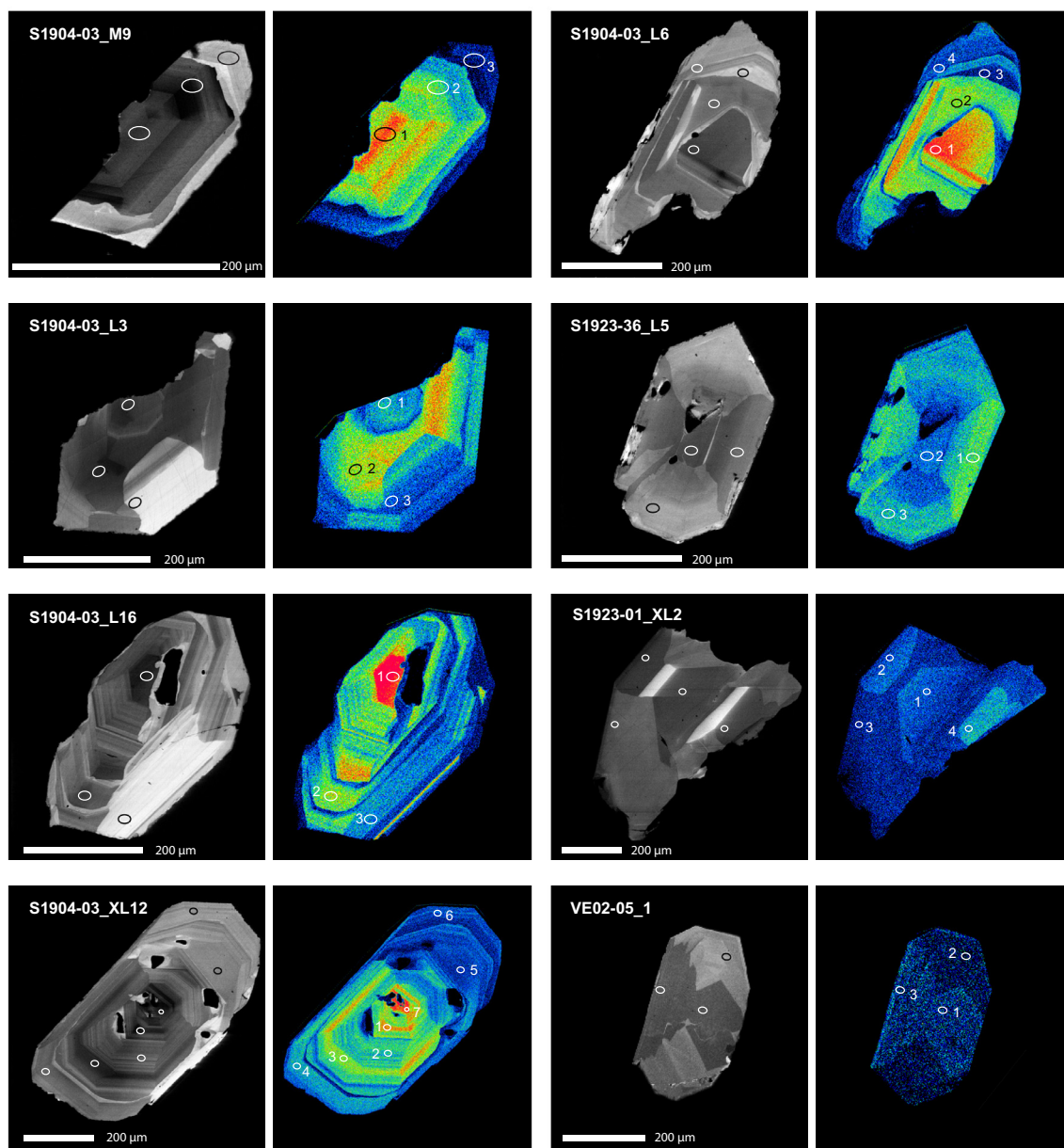


Fig. 1. Cathodoluminescence (CL) images (left) and Y intensity maps (right) of the zircons from this study. SIMS analysis locations are marked in white or black ellipses. For zircon S1904-03\_XL5 see Fig. 2.

(cps) for the indium-mounted zircon compared to 260 cps on experimental zircon with 380 ppmw  $\text{H}_2\text{O}$ . We calculated the detection limit as 15 ppmw  $\text{H}_2\text{O}$  based on  $6\times$  standard deviation of three  $\text{H}^+$  background measurements during the analytical run. Backgrounds for the epoxy-mounted zircons were considerably higher due to outgassing of the epoxy. They averaged to 165–180 cps (based on repeat analyses of zircon 91500<sup>1</sup>) compared to net  $\text{H}^+$  signals on zircon

of 0–400 cps. Therefore, for epoxy-mounted zircons the uncertainty of the water background (ca. 7 cps  $1\epsilon$ ) is the largest source of uncertainty for water analysis, but amounts to less than 2% for the most water-rich zircons. Detection limit based on  $6\times$  standard deviation of the  $\text{H}^+$  background is 55 ppmw for epoxy-mounted zircons.

Trace elements were calibrated using NIST SRM610 using values from Georem (Jochum et al., 2011). Calibration of water was performed using a natural obsidian glass from Lipari with 0.72 wt.%  $\text{H}_2\text{O}$  and 74 wt.%  $\text{SiO}_2$  (unpublished FTIR and XRF data, courtesy of Prof. S. Sparks, University of Bristol) and experimental obsidian glasses from Mangan and Sisson (2000) with corrected  $\text{H}_2\text{O}$  values

<sup>1</sup> Zircon 91500 is not certified anhydrous, but it consistently gave the similar low count rates for  $\text{H}^+$  as experimental ‘dry zircon’ and ‘mudtank’ (Table 2).

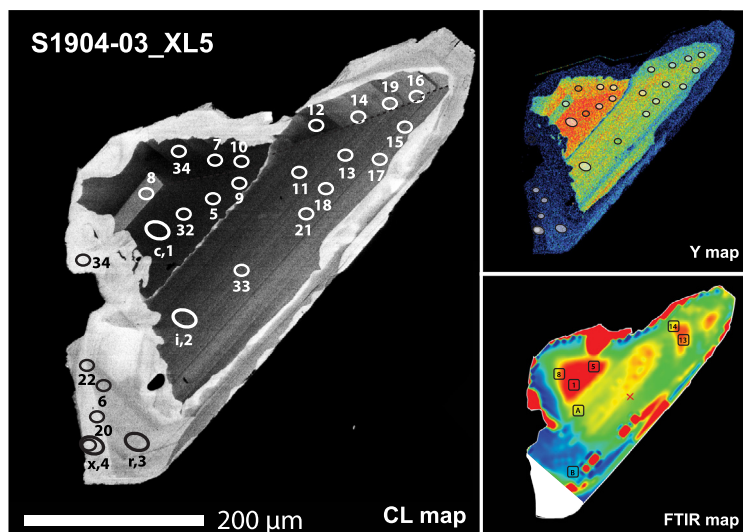


Fig. 2. Cathodoluminescence (CL) image of zircon S1904-03\_XL5 with analytical locations indicated as follows: large white oval: SIMS trace elements (10 nA) + separate H analysis (3 nA), small white oval: SIMS H analysis (3 nA). Stippled lines indicate the boundary between two sector zoning domains. Top-right inset shows Y intensity map of same the grain. Estimated  $Y_2O_3$  concentrations based on ionprobe data indicate that reds represent >1.2 wt.%, yellows 0.8–1.1 wt.%, greens 0.4–0.8 wt.% and blues <0.3 wt.%. Bottom-right inset shows an IR map of the same grain with microFTIR locations for water concentration analysis indicated by black rounded squares. The colours represent the baseline-corrected intensity of the  $3100\text{ cm}^{-1}$  absorbance band. Estimated water concentrations based on unpolarised spectra suggest that red represents >1100 ppm, green 200–300 ppm and blue <80 ppm. The red rim around the very edge of the crystal is an artefact. Note that because FTIR samples the full depth of the crystal, zoning features may appear different from CL and Y maps. (For interpretation of the references to colour in this figure legend, the reader is referred to the web version of this article.)

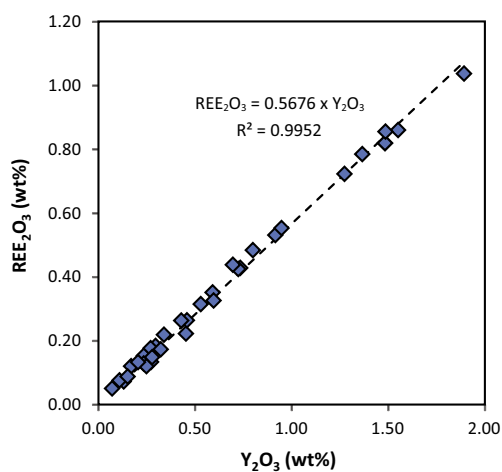


Fig. 3.  $Y_2O_3$  (wt.%) vs.  $REE_2O_3$  (wt.%) contents of zircons.

(T. Sisson, pers. comm.). No correction for  $SiO_2$  content was applied as matrix effects on the ion yield of  $H^+$  relative to  $Si^+$  scale with silica contents of the samples, and therefore the same working curve can be used to calibrate rhyolites, basalts and hydrous minerals (Blundy et al., 2008; Edinburgh Ion Microprobe Facility, unpublished data).

To assess the accuracy of water contents, we analysed synthetic zircons from three separate experiments (see Electronic Supplement). The first (anhydrous) experiment was conducted in a 1 atm furnace; zircons were grown from a slowly cooled ( $\sim 3^\circ/h$ )  $MO_3 + Li_2CO_3$  flux from  $\sim 1400$  to

$\sim 880^\circ C$  using a technique similar to Hanchar et al. (2001). The second was conducted in the  $H_2O-SiO_2-ZrO_2$  system at  $1650^\circ C$  2.5 GPa, in a piston cylinder apparatus, following the procedure of Trail et al. (2011). The final experiment was similar in design, but  $Lu_2O_3$  was added to the starting mix in order to enhance the incorporation of H into zircon through charge compensation. These three experiments yielded zircons with water contents of  $\sim 0$ , 200, and 750 ppmw (Table 2), respectively, as determined by FTIR (Section 2.4) following the methods described in Trail et al. (2011). The experimental zircon grains were subsequently mounted for SIMS analysis by pressing into indium, which resulted in about ten times reduction of  $H^+$  backgrounds. Analytical conditions were identical to those for the natural zircons, but a slightly modified isotope list was used to monitor impurities and the Lu dopant ( $^1H$ ,  $^7Li$ ,  $^{19}F$ ,  $^{24}Mg$ ,  $^{30}Si$ ,  $^{31}P$ ,  $^{40}Ca$ ,  $^{47}Ti$ ,  $^{54}Fe$ ,  $^{89}Y$ ,  $^{91}Zr$ ,  $^{140}Ce$ ,  $^{175}Lu$ ,  $^{178}Hf$ ). CL imaging revealed sector zoning for Lu-doped and the dry zircons, whereas the undoped zircons showed patchy CL patterns (see Electronic Supplement). In Lu-doped zircon a significant difference in Lu and H were identified between sectors, whereas in dry zircon the main difference was in P contents (Table 2). An excellent correlation was observed between  $H_2O$  by SIMS and FTIR, but the values obtained by SIMS are ca. 2 times lower.

The main uncertainty in accuracy of water contents by SIMS is the use of a rhyolite water standard. This calibration strategy gives good results for basaltic glasses (Blundy et al., 2008), which indicates that matrix-induced fractionation is successfully corrected for significantly different matrix compositions using the calibration strategy

Table 2  
Compositions of experimentally grown zircons.

Experiment/zircon	Sector	H <sub>2</sub> O (FTIR)	H <sub>2</sub> O (SIMS)	P	Lu	Li	F	Ca	Mg	Fe	Y	Ce
Dry/z1	CL dark	n.a.	<15	368	10	0.03	16	2.9	0.5	11	54	0.9
Dry/z1	CL bright	n.a.	20	143	16	0.03	12	5.3	0.5	5	82	0.3
Mudtank <sup>a</sup>	–	20	<15	50	1.5	0.04	19	1.7	1.0	8	36	1.4
mudtank	–	20	<15	45	0.9	0.08	16	3.8	0.7	11	41	1.2
zw68/z1	–	213	97	12	0.1	0.01	26	6.7	28.7	11	0.9	0.6
zw73/z1	Core	855	381	12	6300	0.02	14	5.7	1.6	7	0.8	0.4
zw73/z1	Core	855	388	13	6352	0.02	10	6.5	1.8	9	0.7	0.5
zw73/z1	CL dark	855	367	14	6026	0.02	14	4.9	1.5	10	0.6	0.7
zw73/z1	CL bright	n.a.	242	19	3778	0.05	16	17.8	6.1	10	0.5	0.7
zw73/z1	CL bright	n.a.	245	18	3900	0.02	20	6.7	2.0	8	0.4	0.7
zw73/z2	CL bright	750	354	32	6092	0.01	23	5.1	4.1	8	1.0	0.5

All concentrations in ppmw. n.a. = not analysed.

<sup>a</sup> Gem-quality zircon from Mud Tank carbonatite, Australia.

described above. Limited matrix-induced fractionation for H<sub>2</sub>O (<30%) was observed amongst various hydrous silicate minerals and silicate glasses (biotite, arfvedsonite, cordierite, clinohumite, serpentine; EIMF unpublished data), similar to findings by [Ottolini et al. \(2002\)](#). Although this does not imply that no matrix-induced fractionation exists for H between rhyolite and zircon, an offset of a factor two would be unexpected.

The main source of uncertainty in accuracy of water contents of zircon by FTIR is the absorption coefficient. The value published by [Bell et al. \(2004\)](#) of 4730 L mol<sup>-1</sup> cm<sup>-2</sup> is based on unpublished NRA analyses of kimberlitic zircon, but contained a math error; a corrected value of 36,241 L cm<sup>-2</sup> mol<sup>-1</sup> was published by [Trail et al. \(2011\)](#). We suspect the unpublished NRA measurement on which this value is based may have been in error. A re-evaluation of the absorption coefficient based on new NRA measurements of REE-bearing zircons is in progress.

#### 2.4. FTIR

MicroFTIR transmitted light spectra of grain S1904-03\_XL5 (resting in BaF disk after removal from epoxy puck) were collected at Bristol University on a Thermo Nicolet iN10 spectrometer using a MCT/A detector and KBr beamsplitter. For E//a and E//c spectra a ZnSe polariser was used and 256 scans collected at a resolution of 4 cm<sup>-1</sup> through an aperture of 30 × 30 microns. The polished surface of the zircon was found to be very close to parallel to the c-axis as determined by EBSD (see Section 2.5). Polarised FTIR spectra //a and //c closely matched those of [Woodhead et al. \(1991b\)](#) and [Trail et al. \(2011\)](#). H<sub>2</sub>O contents were calculated using the method detailed by [Trail et al. \(2011\)](#) using total integrated absorbance per centimeter, calculated from polarised spectra in the two principal optical directions *a* and *c*. However, this method did not include absorption below 3000 cm<sup>-1</sup>, whereas our spectra show a clear feature at ~2950 cm<sup>-1</sup>. Incorporation of this feature in the water contents by extending the integrated range to 2600 cm<sup>-1</sup> increases the concentrations by about 15%. Note that combination bands around 2750 cm<sup>-1</sup> are insignificant even in the most water-poor zircons. An FTIR map of grain S1904-03\_XL5

was made using an automated stage to give a 10 μm step grid. Each unpolarised spectra was acquired through a 10 × 10 μm aperture with 32 scans at 8 cm<sup>-1</sup> spectra resolution.

#### 2.5. Electron backscatter diffraction

The crystallographic orientation relative to the polished surface of zircon grain S1904-03\_XL5 was determined by electron backscatter diffraction (EBSD) using the Oxford Instruments AZtec electron backscatter diffraction (EBSD) system on a Carl Zeiss SIGMA HD VP Field Emission SEM at EMMAC, University of Edinburgh. For several points on the grain the diffraction pattern was collected and solved by the software for the orientation of zircon. Prior to EBSD analysis the sample was polished with colloidal silica in order to remove damage to the surfaces caused by earlier mechanical polishing. The *c* axis of zircon grain S1904-03\_XL5 was oriented parallel to the polished surface within a few degrees (see [Electronic Supplement](#)).

### 3. RESULTS

#### 3.1. Trace elements and zoning patterns

Trace element contents of the nine Vema zircons are presented in [Table 3](#) and the [Electronic Supplement](#). The zircons show a large range of Y (0.07–1.76 wt.%) and ΣREE<sup>2</sup> (0.05–1.04 wt.%) contents, which mirror the zoning features visible in cathodoluminescence (CL) images ([Figs. 1 and 2](#)). Most zircons have REE-enriched cores and REE depleted rims (M9, L3, XL5, XL12, L6, L16) and usually show regions with oscillatory zoning patterns. Sector zoning is frequently observed (XL5, L5, XL2, VE1). Some zircons show CL bright, REE-poor recrystallised rims (XL5, M9), domains (L3, L16) or fracture fillings (XL5, L5, L6), probably due to deuteric alteration (cf. [Grimes et al., 2009](#)). Zircons XL5 and XL2 show CL-bright small

<sup>2</sup> From here on, REE will include Y unless Y is mentioned separately. ΣREE represents the sum of all individual REE including Y unless mentioned separately.

Table 3  
Trace element compositions of two zircons from sample S1904–03 by SIMS.

Zircon domain	L16			XL5			
	Core	Mantle	Rim	Core	Mantle	Rim	Rim2
<i>wt.%</i>							
SiO <sub>2</sub>	32.60	32.60	32.60	32.60	32.60	32.60	32.60
HfO <sub>2</sub>	1.57	1.64	1.53	1.64	1.58	1.51	1.39
P <sub>2</sub> O <sub>5</sub>	0.55	0.33	0.26	0.42	0.29	0.13	0.06
P <sub>2</sub> O <sub>5</sub> <sup>a</sup>	na	na	na	0.49	0.34	0.16	0.07
<i>ppmw</i>							
H <sub>2</sub> O <sup>a</sup>	1201	291	70	1212	683	<55	<55
Li	<0.01	<0.01	0.4	<0.01	<0.01	<0.01	<0.01
Mg	0.1	0.3	0.4	na	na	na	na
Al	<0.1	0.4	6.2	na	na	na	na
Ca	0.6	0.9	3.6	3.1	25.2	0.2	11.4
Ti	11.4	13.0	6.4	10.8	8.8	6.9	3.6
Fe	5.5	5.7	7.0	na	na	na	na
Nb	9.1	8.6	2.4	na	na	na	na
Ba	0.06	0.09	0.16	<0.05	0.29	0.27	0.23
Y	14930	5775	2660	11720	7465	1840	530
Y <sup>a</sup>	13845	5585	2720	11880	7805	1980	735
La	0.145	0.026	0.027	0.073	0.029	0.009	0.025
Ce	96.4	49.4	7.6	72.3	36.6	8.7	3.7
Pr	1.2	0.19	0.037	1.07	0.52	0.045	0.045
Nd	22.5	3.8	1.2	19.1	9.8	1.05	0.094
Sm	41.6	10.2	3.0	35.0	19.4	2.5	0.52
Eu	10.2	3.4	1.01	7.9	4.6	0.65	0.19
Gd	233	73	26	187	110	17	3.4
Tb	97	33	13	78	46	9.1	2.1
Dy	1080	395	165	874	532	113	29
Ho	447	171	80	372	233	54	15
Er	2130	854	419	1754	1109	282	83
Tm	446	187	99	369	243	67	20
Yb	3688	1599	878	3043	2027	615	207
Lu	825	370	216	701	481	155	51
Th	303	284	8.0	258	112	8.9	1.02
U	201	169	29	157	97	30	8.2
<i>Sum of charge</i>							
ΣY + REE	222	87	41	176	113	28	8
P	78	46	37	60	41	18	8
H	132	32	8	134	75	4	4
ΣM <sup>1,2,3,5+</sup>	0	0	1	0	1	0	1

<sup>a</sup> Elements measured separately during a second analysis in same location with smaller beam (Section 2.3). Analysis locations are shown in Fig. 1 (L16) and Fig. 2 (XL5). Sum of charge calculated as ppmw/atomic weight × (cation charge – 4). ΣM<sup>1,2,3,5+</sup> represents cation charge of all non-tetravalent trace elements excluding H, P and REE.

rectangular core domains, which are poor in REE compared to adjacent CL-darker domains. Despite the complexity of features, most zircons do not contain xenocrystic cores and appear to have undergone a continuous magmatic growth history, occasionally followed by small amounts of late-stage deuteric alteration.

The REE patterns are typical of igneous zircon (Fig. 4), with strongly depleted LREE, strong positive Ce anomalies (Ce/Ce\* = 10–255) and negative Eu anomalies (Eu/Eu\* = 0.2–0.6). The patterns are subparallel, i.e., despite the large range in REE concentrations the patterns are very similar. In addition to large variations in ΣREE contents, the zircons show a large range in P<sub>2</sub>O<sub>5</sub> (0.05–0.55 wt.%), Th (1–2606 ppmw) and U (8–269 ppmw). HfO<sub>2</sub> contents range from 1.06 wt.% to 2.08 wt.%. Other elements are

present in very small amounts (Ti 4–19 ppmw, Ca 0.1–42 ppmw, F 3–15 ppmw, Li < 0.4 ppmw, Mg < 1 ppmw, Al < 7 ppmw, Fe < 7 ppmw, Nb < 10 ppmw). The concentrations fall within the range of those from oceanic lithosphere (Cavosie et al., 2009; Grimes et al., 2009), but appear more evolved than average Fe–Ti oxide gabbros from these authors, extending well into their plagiogranite field. The Th and U contents of these zircons indicate that they received a radiation dose D<sub>α</sub> of 4 × 10<sup>15</sup> to 1 × 10<sup>18</sup> α decay events/g, well below the radiation damage threshold (Murakami et al., 1991).

The cations that constitute the zircon structure (Zr, Si) are tetravalent, thus incorporation of non-tetravalent cations will require charge-balancing cation-exchange reactions. The most abundant non-tetravalent cations are

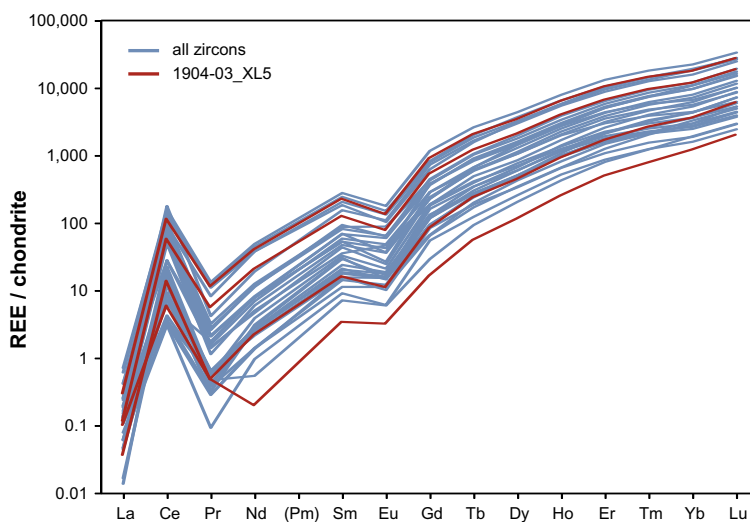


Fig. 4. Chondrite-normalised REE patterns of zircons.

$\Sigma$ REE and P, which show a strong positive correlation (Fig. 5A). However, in nearly all zircons,  $P_2O_5$  contents are too low to completely charge-balance trivalent element contents, with  $P_2O_5$  concentrations generally about half of those required to provide charge balance (Fig. 5A).

### 3.2. Zircon water contents and structural position

The water contents of zircons as measured by SIMS range from values near the detection limit (ca. 25 ppmw  $H_2O$ ) up to 1212 ppmw  $H_2O$  (Tables 3 and 4). The range in water contents is large for most individual zircons and shows a clear positive correlation with  $P_2O_5$  and  $\Sigma$ REE contents (Fig. 5B and D). Recrystallised rims have lowest H and REE. To study the relationship between trace element patterns and water contents in detail, 21 analyses were performed on a single zircon, S1904-03\_XL5. This zircon shows several zoning patterns, including normal, oscillatory and sector zoning (Fig. 2). It also includes a distinct core domain as well as a recrystallised rim. The range of water contents of this single zircon (<15 to 1212 ppmw) nears the range of that of the whole zircon suite (Fig. 5B) and shows distinct water- $\Sigma$ REE-P trends for different sectors and domains, which are discussed in detail in Section 4.1.

The same grain (S1904-03\_XL5; Fig. 2) was also analysed by FTIR (after removal from the epoxy mount). The FTIR spectra show a highly oriented absorption band //a at  $3105\text{ cm}^{-1}$  with a smaller unresolved band at  $3200\text{ cm}^{-1}$  (Fig. 6). A hump in the tail of the  $3105\text{ cm}^{-1}$  band is observed at  $2930\text{ cm}^{-1}$  and a small additional band can be seen at  $2450\text{ cm}^{-1}$ . As all spectra are similar irrespective of total absorbance, the water site is the same regardless of water content. The water contents range from 2014–2359 ppmw near the core to 93–108 ppmw in the recrystallised rim (Table 4). The size of the main  $3105\text{ cm}^{-1}$  absorption band scales with REE,  $H_2O$  and  $P_2O_5$  contents measured by SIMS, although direct comparison is hampered by the different sampling volumes of the techniques (SIMS only samples the upper few  $\mu\text{m}$  of the

grain, whereas FTIR samples the full depth, which was 79  $\mu\text{m}$ ) and the large fine-scale variability of trace element contents in this zircon grain (Fig. 2). A comparison between SIMS and FTIR suggests about a factor two difference in the water contents measured by the two methods (Table 4). We suspect this is mainly related to uncertainty in the FTIR absorption coefficient (see Section 2.3).

The narrow absorption bands confirm that this zircon has received a low radiation dosage and is not metamict, as metamict zircons have broad and non-polarised absorption bands stretching from  $3600$  to  $2900\text{ cm}^{-1}$  (Woodhead et al., 1991b; Nasdala et al., 2001; Zhang et al., 2002). This is also supported by the presence of very small but distinct combination mode peaks at  $2750\text{ cm}^{-1}$  in E//c spectra of the most  $H_2O$ -poor region of the zircon (cf. Woodhead et al., 1991b). The FTIR pattern is nearly identical to the ‘crystalline S.E. Asia zircon’ from Woodhead et al. (1991b). Compared to experimentally grown water-bearing zircons (this study; Trail et al., 2011), our spectra closely match those of Lu-doped zircons, which have the strongest band at  $3113\text{ cm}^{-1}$  and a smaller band at  $\sim 3200\text{ cm}^{-1}$  (Fig. 5). Other spectra, including those of zircons doped with Th, Al and Ti plus undoped experiments, do not show the main  $\sim 3100\text{ cm}^{-1}$  band (Trail et al., 2011). Vice versa, strong bands at  $3384$  and  $3418\text{ cm}^{-1}$  observed in zircons from kimberlites and undoped experiments (Trail et al., 2011) were not visible in our sample.

## 4. DISCUSSION

### 4.1. Water incorporation mechanism

The main substitution reaction in zircon for cations other than tetravalent cations, such as Hf, U, Th and Ti, is the xenotime reaction (Speer, 1980; Finch et al., 2001):



However, in many natural zircons the amount of P is often insufficient to charge-balance all REE (Belousova et al.,

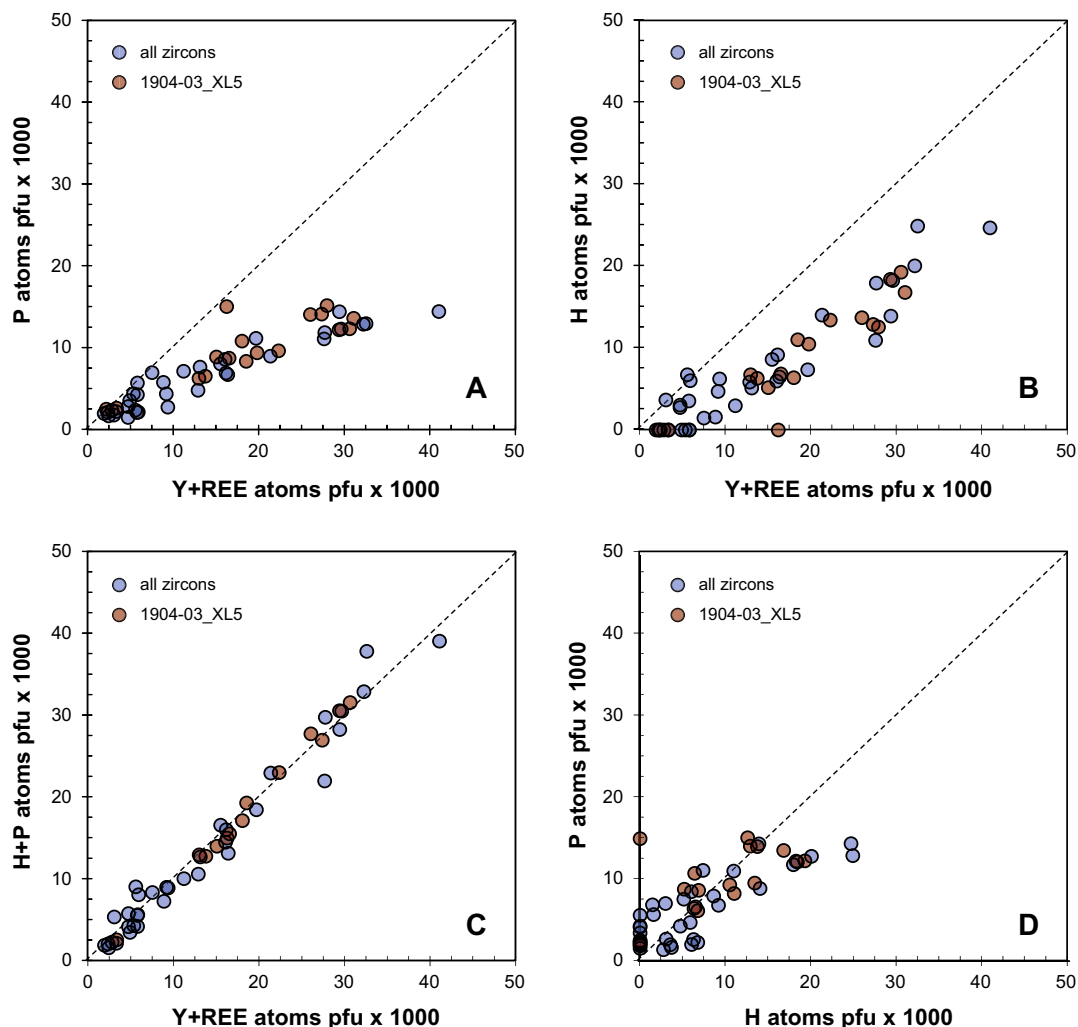


Fig. 5. Variation diagrams for H, P and REE. Values are given as atoms per functional zircon unit based on 40 multiplied by 1000. Values for  $H < \text{d.l.}$  have been plotted as zero. (A) P vs. REE + Y; (B) H vs. REE + Y; (C) H + P vs. REE + Y, and (D) P vs. H.

2002; Hoskin and Schaltegger, 2003), including the zircons from this study (Fig. 7). Other trace elements that can potentially balance this charge deficit (such as Al, Fe, Mg, Li; Hancher et al., 2001; Hoskin and Schaltegger, 2003) are too low in abundance to in the Vema zircons, contributing  $<2\%$  of the total charge compared to REE (Table 3). In contrast, H contents of zircons are close to those expected for charge balancing the P deficit (Fig. 5C) and show strong positive correlations with REE and  $\text{P}_2\text{O}_5$  in Vema zircons. This indicates a possible coupled substitution mechanism for these elements. Although co-variation of elements does not necessarily imply a coupled substitution, as similar trends can be created if elements exhibit similar geochemical behaviour (e.g., comparable bulk-melt distribution coefficients), the Vema zircon data strongly suggest that REE–P–H contents are controlled by charge balance.

Hence, we propose that charge balance in the Vema zircons is achieved through a combination of the common xenotime substitution (Eq. (1)) with the following

substitution mechanism (Woodhead et al., 1991b; Nasdala et al., 2001; Hinton et al., 2003; Trail et al., 2011):



The two substitution mechanisms (Eqs. (1) and (2)) do not operate equally in all zircons, as the H/P atomic ratio range is substantial (0.03–3.64, averaging 1.11) and increases with increasing  $\Sigma\text{REE}$  substitution (Fig. 5D). In recrystallised rim and low-REE core domains,  $\text{H}_2\text{O}$  contents are very low and charge balance is nearly completely maintained by xenotime substitution. Sector zoning also affects REE, H and P distribution, as the REE-depleted sectors in crystal S1904-03\_XL5 has higher P but lower H, REE and H + P than the REE-enriched sectors (Fig. 8). The contrasting behaviour of REE and P is particularly interesting, as typically sector zoning is regarded to increase all trace elements in one particular sector compared to another (Watson and Liang, 1995). Our data suggests that this is due to non-equilibrium effects, which be discussed further in Section 4.3.2.

Table 4

Water, P<sub>2</sub>O<sub>5</sub>, Y<sub>2</sub>O<sub>3</sub> and  $\Sigma$ REE<sub>2</sub>O<sub>3</sub> contents of zircon S1904-03\_XL5 by SIMS and FTIR.

Analysis	Domain	P <sub>2</sub> O <sub>5</sub> wt.%	Y <sub>2</sub> O <sub>3</sub> wt.%	$\Sigma$ REE <sub>2</sub> O <sub>3</sub> wt.% <sup>a</sup>	H <sub>2</sub> O ppmw <sup>b</sup>	H <sub>2</sub> O ppmw <sup>c</sup>	H <sub>2</sub> O ppmw <sup>d</sup>
XL5-1	Sector 1	0.49	1.51	0.84	1212	1605	1876
XL5-2	Sector 1	0.34	0.99	0.55	683		
XL5-3	Overgrowth	0.16	0.25	0.14	<55	93	108
XL5-4	Overgrowth	0.07	0.09	0.05	<55		
XL5-5	Sector 1	0.47	1.42	0.79	939	2014	2359
XL5-6	Overgrowth	0.10	0.16	0.09	<55	445	532
XL5-7	Sector 2	0.54	1.27	0.71	627		
XL5-8	Core	0.57	0.75	0.42	<55	846	972
XL5-9	Sector 1	0.46	1.36	0.76	896		
XL5-10	Sector 2	0.54	1.21	0.67	668		
XL5-11	Sector 1	0.37	1.04	0.58	653		
XL5-12	Sector 2	0.41	0.84	0.47	310		
XL5-13	Sector 1	0.32	0.86	0.48	536	1001	1211
XL5-14	Sector 2	0.34	0.70	0.39	251	845	1013
XL5-15	Sector 1	0.25	0.64	0.36	307		
XL5-16	Sector 2	0.33	0.77	0.43	333		
XL5-17	Sector 1	0.24	0.60	0.34	328		
XL5-30 <sup>e</sup>	Sector 2	0.58	1.30	0.72	609		
XL5-32 <sup>e</sup>	Sector 1	0.52	1.44	0.80	815		
XL5-33 <sup>e</sup>	Sector 1	0.36	0.92	0.51	507		
XL5-34 <sup>e</sup>	Overgrowth	0.09	0.11	0.06	<15		

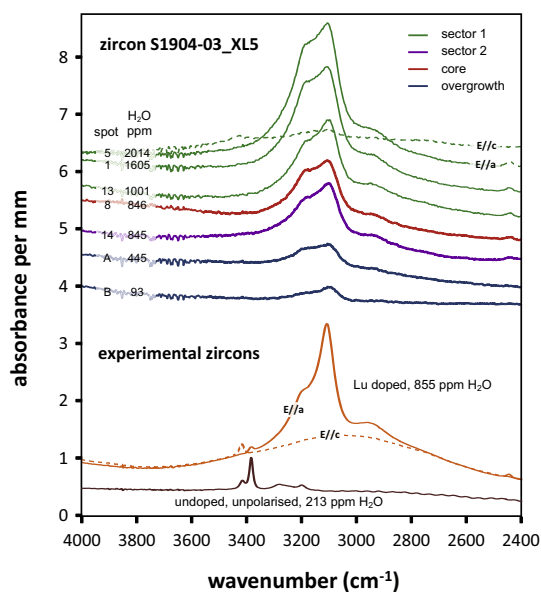
<sup>a</sup> Calculated from Y<sub>2</sub>O<sub>3</sub> contents following the equation in Fig. 2.<sup>b</sup> SIMS data.<sup>c</sup> FTIR data integrating 3550–3000 cm<sup>-1</sup>.<sup>d</sup> FTIR data integrating 3550–2600 cm<sup>-1</sup>.<sup>e</sup> Grain remounted in indium with lower H<sub>2</sub>O detection limit of 15 ppmw. Analysis locations are shown in Fig. 2. Analyses XL5\_1 to XL5\_4 match those listed for zircon XL5 in Table 2.

Fig. 6. Zircon FTIR spectra of various analysis spots on grain S1904-03\_XL5 and for experimentally grown zircons. Spectra have been vertically displaced for clarity. Analysis locations for grain S1904-03\_XL5 can be found in Fig. 2. Calculated water content of each spot is indicated for each spectrum (see Section 2.4 for details of calculation). Experimental zircons are ‘undoped’ and ‘Lu-doped’ hydrous zircons (Table A1).

FTIR data also supports a coupled substitution with REE, as the absorption spectra of Vema zircons closely

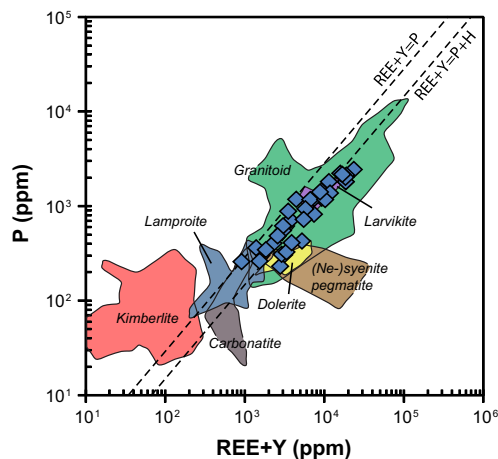


Fig. 7. REE + Y vs. P diagram showing compositions of zircons of various provenance (Belousova et al., 2002) and Vema zircons from this study. Also indicated are lines for which the total amount of REE + Y is charge balanced by (1) P only and (2) H + P in equal atomic proportions.

match those of Lu-doped experimental zircons (Fig. 6). Data from undoped experimental zircons indicates that only up to 200 ppmw H<sub>2</sub>O can enter the zircon structure (at 1650 °C, 2.5 GPa; this study, Trail et al., 2011), whereas doping with trace elements, including REE, strongly increased the zircon water contents, providing clear evidence for a coupled substitution mechanism.

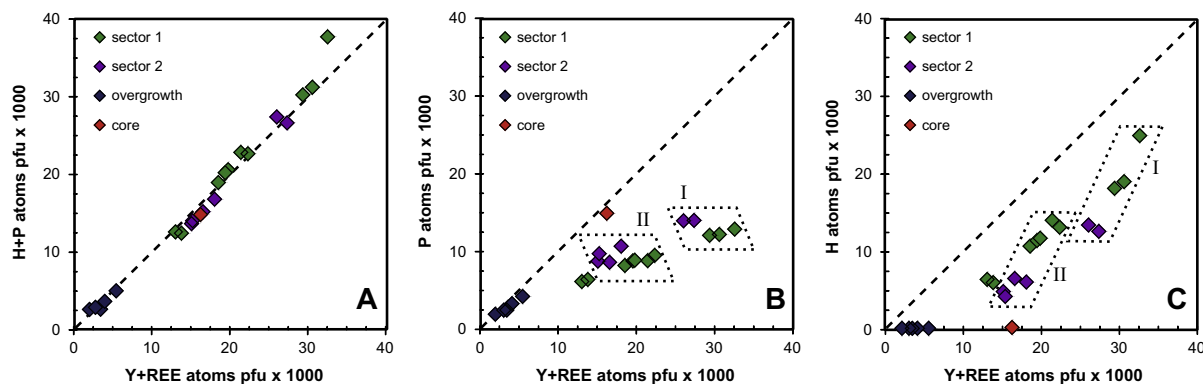


Fig. 8. Variation diagrams for H, P and REE for zircon S1904-03\_XL5, detailing the effects of sector zoning. Values are given as atoms per functional zircon unit based on 4O multiplied by 1000. Values for H < d.l. have been plotted as zero. (A) H + P vs. REE + Y; (B) P vs. REE + Y, and (C) H vs. REE + Y.

One intriguing aspect of the Vema zircon FTIR data is the absence of commonly reported OH bands at  $\sim 3400\text{ cm}^{-1}$ . Woodhead et al. (1991b) argued that sharp peaks at  $3420\text{ cm}^{-1}$  (E//c) and  $3385\text{ cm}^{-1}$  (E $\perp$ c) mark the OH site in zircon, and that the absence of this peak meant that the zircon was anhydrous. Our data disprove this, as the Vema zircons lack the  $3400\text{ cm}^{-1}$  peak despite having high water contents. Trail et al. (2011) speculated that the  $3400\text{ cm}^{-1}$  peak represented an OH site related to a Zr vacancy and suggested that the  $3200\text{ cm}^{-1}$  band is related to a hydrogrossular substitution (Si vacancy:  $\text{SiO}_4 = [\ ](\text{OH})_4$ ). As the  $3200\text{ cm}^{-1}$  band is clearly present in our spectra, and no vacancies are created in the two charge-balancing exchange reactions (Eqs. (1) and (2)), we infer that this band is probably not vacancy related. This is supported by a recent molecular dynamics study which calculated the most stable configurations of OH incorporation and associated OH bond lengths, from which FTIR absorption bands can be predicted (Botis et al., 2013). The authors concluded that the  $3100\text{ cm}^{-1}$  and  $3220\text{--}3250\text{ cm}^{-1}$  peaks are related to substitution mechanism Eq. (2), where the hydrogen ion can be either in a position close to the  $\text{M}^{3+}$  cation ( $3220\text{--}3250\text{ cm}^{-1}$  band) or a far position ( $3100\text{ cm}^{-1}$  band). Both peaks are observed in the Vema zircons (Fig. 6). The study also assigned the (partial) hydrogrossular substitution to a  $3420\text{ cm}^{-1}$  band. As this mechanism involves a Si vacancy, it seems reasonable to assume that it most likely occurs in rocks with low silica activities such as kimberlites, as is the case for, e.g., olivine (Berry et al., 2005). The available literature appears to confirm this (Woodhead et al., 1991b; Bell et al., 2004), which may explain the lack of this mode of OH incorporation in our zircons, which are from rocks with high silica activities. In addition, zircons from kimberlites commonly show an excess P over REE (Belousova et al., 2002), so no H is needed for charge balance (Fig. 7). We note, however, that the  $\sim 3400\text{ cm}^{-1}$  band is nearly absent in Lu-doped experiments from Trail et al. (2011), but does appear in non-doped experiments, despite similar starting materials and experimental conditions. This suggests that the hydrogrossular substitution may be suppressed in the presence of REE + H substitution.

#### 4.2. Maximum water and REE contents of non-metamict zircons

The maximum amount of water that can be incorporated in zircons for a given pressure, temperature and water activity in the melt has yet to be determined, but is perceived to be very limited, e.g., 0.01 wt.% by Woodhead et al. (1991b). This in contrast to metamict zircon, that can contain larger amounts of structural water (up to 0.04 wt.%, Woodhead et al., 1991a) plus significant amounts of secondary water (Nasdala et al., 2001; Zhang et al., 2002). Here we report maximum water contents of 0.12 wt.%  $\text{H}_2\text{O}$  in REE-rich crystalline zircons, indicating that such water contents cannot simply be used to infer a metamict state of the zircon without knowledge of its REE contents or IR spectral evidence of the OH site (Cliff et al., 2013). This is supported by experimental data by Trail et al. (2011), who showed that very high  $\text{H}_2\text{O}$  contents ( $>0.17\text{ wt.}\%$ ) can be accommodated by REE-rich crystalline zircon, perhaps aided by the high  $P\text{--}T$  conditions of the experiments ( $1650\text{ }^\circ\text{C}$ , 2.5 GPa). The upper water limit may be determined by increased lattice strain at the Zr site during incorporation of REE, as REE are larger than Zr ( $^{87}\text{Zr}^{4+}$  0.84 Å,  $^{87}\text{Y}^{3+}$  1.02 Å). During the xenotime substitution this is partially balanced by substitution of the smaller P cation on the Si site ( $^{43}\text{Si}^{4+}$  is 0.26 Å vs.  $^{43}\text{P}^{5+}$  is 0.17 Å) (Finch et al., 2001), but the incorporation of H will have no such effect and results in increased lattice strain. One would therefore expect for H/P ratios to decrease with increasing H and REE contents, but we observe the opposite although the data is rather scattered (Fig. 5).

Similarly, Hoskin and Schaltegger (2003) state that zircon analyses with significantly more than 1 wt.% Y +  $\Sigma\text{REE}$  must be the result of alteration or contamination by accidental analysis of inclusions. However, the Y + REE content of Vema zircons reaches a maximum of 2.94 wt.%, an amount which is completely charge-balanced by  $\text{P}_2\text{O}_5$  and  $\text{H}_2\text{O}$  (0.55 wt.% and 1201 ppmw, respectively). Even higher REE + Y contents (up to ca. 5 wt.%) were reported by Grimes et al. (2009), but no H contents were reported by the authors. If REE in zircon were due to

accidental analysis of xenotime inclusions, the zircons would plot on the 1:1 line in Fig. 7, whereas in fact most plot below this line. Therefore, although the upper limit of REE solubility in zircon is poorly constrained, our results demonstrate that it is strongly dependent on P and H activities in the system and extends to much higher values than has been previously suggested.

### 4.3. Implications for the use of zircon to estimate melt water contents and zircon REE partitioning

#### 4.3.1. Equilibrium partitioning

An important outstanding issue is whether H in zircon can be used to constrain the water activity of melt (e.g., Trail et al., 2011). As H uptake in zircon is in a charge-balance mechanism with REE and P, the contents of the latter need to be taken into account. The concentration of a trace element  $i$  in the melt can be estimated from its concentration  $c_i$  in a mineral and an experimentally determined distribution coefficient  $D_i$ , assuming other elements exert no influence on the distribution of element  $i$ . However, if element  $i$  is part of a coupled substitution with element  $j$ , the concentration  $c_j$  of the latter must be taken into account. For a reaction  $i_{\text{melt}} + j_{\text{melt}} = i_{\text{mineral}} + j_{\text{mineral}}$ , we can write an equilibrium equation:

$$\frac{c_{\text{min}}^i \times c_{\text{min}}^j}{c_{\text{melt}}^i \times c_{\text{melt}}^j} = K_D \quad (3)$$

Thus, the concentration, or more accurately, the activity of H in zircon, as incorporated following Eq. (2), depends on REE activity of the melt as follows:

$$(\text{H})_{\text{zrc}} = \frac{K_{D1}(\text{H})_{\text{melt}}(\text{REE})_{\text{melt}}}{(\text{REE})_{\text{zrc}}} \quad (4)$$

assuming constant activities of Zr in zircon and the melt. The latter assumption is valid when zircon saturation is reached. Note that to satisfy charge-balance constraints,  $[\text{H}]_{\text{zrc}} = [\text{REE}]_{\text{zrc}}$ . A similar equation can be written for P and REE in the xenotime reaction Eq. (1), ignoring the presence of water:

$$(\text{P})_{\text{zrc}} = \frac{K_{D2}(\text{P})_{\text{melt}}(\text{REE})_{\text{melt}}}{(\text{REE})_{\text{zrc}}} \quad (5)$$

assuming constant activities of Zr and Si in melt and zircon. If both H and P are present, they compete for REE to obtain charge balance in zircon and the concentrations of all three elements in zircon are mutually dependent on their concentrations in the melt. The ratio of H and P in zircon is equal to  $K_{D1}/K_{D2}$ .

As Eqs. (4) and (5) are essentially the same, the combined solubility of H + P can be expressed, as a first approximation, as:

$$(\text{H} + \text{P})_{\text{zrc}} = \frac{K_{D3}(\text{H} + \text{P})_{\text{melt}}(\text{REE})_{\text{melt}}}{(\text{REE})_{\text{zrc}}} \quad (6)$$

where  $K_{D3} = f_{\text{H}} \times K_{D1} + (1 - f_{\text{H}}) \times K_{D2}$  with  $f_{\text{H}} = (\text{H})/(\text{H} + \text{P})_{\text{melt}}$  and the ratio of H and P in zircon is proportional to that in the melt:

$$\frac{(\text{H})_{\text{zrc}}}{(\text{P})_{\text{zrc}}} = k \frac{(\text{H})_{\text{melt}}}{(\text{P})_{\text{melt}}} \quad (7)$$

This set of equations allows us to calculate the concentration of H, P and REE in zircon based on their concentrations in the melt, if  $K_{D1}$  and  $K_{D2}$  are known and assuming activity factors of one. An important consequence of the above formulation is that the same zircon composition can be derived from different melt compositions, so for a given water content of zircon, the water content of the melt can only be constrained if either REE or P content of the melt can be determined independently. Note that although our treatment differs in detail from that by Wood and Blundy (2001), as their model is based on the composition of the crystal and not the melt, they also predicted matrix-dependent  $D$  values for charge-coupled substitutions.

An additional consideration is the activity of H in the melt, as water dissolves as hydroxyl ( $\text{OH}^*$ ) and molecular water ( $\text{H}_2\text{O}^*$ ) in siliceous melts (Stolper, 1982; Zhang, 1999). The relative proportions of the two water species depend on the total water content of the melt; at low water contents most  $\text{H}_2\text{O}$  dissolves as  $\text{OH}^*$ , but  $\text{H}_2\text{O}^*$  becomes increasingly important with increasing water contents and above about 3–5 wt.%  $\text{H}_2\text{O}$ , most water dissolves as  $\text{H}_2\text{O}^*$  (Ihinger et al., 1999; De Hoog et al., 2009). As water is incorporated into zircon as hydroxyl, partitioning of H between zircons and melt could be affected by this speciation change.

The interdependence of P, H and REE has important implications for REE zircon-melt partitioning studies. It has been noted that  $D$  values determined from natural samples and experimental studies vary by at least two orders of magnitude (Hanchar and van Westrenen, 2007). The authors indicate several possible reasons, including zoning of crystals, analytical difficulties, presence of REE-rich accessory phases and melt structure. However, as shown in Eqs. (4) and (5), the Nernst equation for partition coefficients does not apply when charge balance is needed to incorporate a certain trace element. Only if charge balance is maintained by exchange for major elements, the concentrations of which can be assumed approximately constant in many systems (e.g., REE in augite through the reaction  $\text{REE} + \text{Al} = \text{Ca} + \text{Si}$ ), can a charge-balance coupled substitution be approximated by a constant  $D$  value. However, in the case of REE in zircon, the concentrations of  $\text{H}_2\text{O}$  and  $\text{P}_2\text{O}_5$  vary widely between different natural systems and change significantly during magma evolution, and therefore so will  $D$  values. For instance,  $D_{\text{zrc/melt}}^{\text{REE}}$  increases with increasing H and P contents of the melt, whereas  $D_{\text{zrc/melt}}^{\text{H}}$  increases with increasing REE content but decreases with increasing P content. This makes inferring melt water contents from H in zircon particularly challenging.

#### 4.3.2. Kinetic effects

The solution model presented in Section 4.3.1 assumes equilibrium partitioning of H, P and REE during zircon growth. However, all zircons from this study show oscillatory zoning and/or sector zoning (Figs. 1 and 2). Oscillatory zoning may be the result of external forcing,

e.g., magma mixing, convection or volatile release, or intrinsic crystal growth processes related to varying diffusivities of major and trace elements in the boundary layer surrounding the growing crystal (Hoskin, 2000; Fowler et al., 2002). As diffusivities of most elements in zircon are low, oscillatory zoning will be preserved during continued crystal growth (Watson and Liang, 1995).

Sector zoning has been related to different crystal faces having different bonding energies and therefore differential uptake of trace elements from the melt (Dowty, 1976). Whether the occurrence of sector zoning is related to crystal growth rate is disputed (Watson and Liang, 1995), but growth rates of different sectors vary and therefore any crystal growth-rate related effects such as boundary layer diffusion will be amplified.

In Vema zircon S1904-03\_XL5, H and REE are highest in the slow growing sector (CL dark, //c-axis), whereas P is highest in the fast growing sector (Fig. 8). Although P contents of the melts are unknown, they were likely to be higher than P contents of the zircons ( $P_2O_5 = 0.05\text{--}0.55$  wt.%) as the melts were apatite saturated. Therefore, P was present in excess near the growing zircon crystal and needed to diffuse away during zircon growth. The same applies to H, as it must have been in excess in the melt, but REE (with the exception of LREE) are enriched in zircon relative to the melt and thus needed to diffuse towards the growing zircon. As P is one of the slowest diffusing elements in silicate melts (Harrison and Watson, 1984), during rapid crystal growth P will be unable to diffuse away from the growing crystal surface and become trapped, leading to excess P in zircon. Due to the excess P, less H is needed to charge balance REE and H/P will decrease in the faster growing sector, as is indeed observed (Fig. 8). One would expect the REE concentration to increase to compensate for the increased P contents, but in reality REE decrease in the P-rich sectors (Fig. 8). This suggests that perhaps REE incorporation is also diffusion limited.

It is difficult to constrain if the H–P–REE systematics observed for sector zoning also characterise oscillatory zoning, as the oscillations are too narrow to be measured individually as well as superimposed on a strong normal zoning pattern. The overall fractionation trend of the zircons is a simultaneous decrease of H, P and REE, which differs from the sector zoning and is consistent with the equilibrium fractionation model.

#### 4.3.3. Implications for REE patterns

The shape of REE patterns is probably relatively unaffected by the fractionation effects indicated above and may therefore still provide useful genetic information about the source rock (e.g., Belousova et al., 2002). Important potential exceptions are Ce and Eu anomalies. Cerium anomalies are common in zircon due to the preferential uptake of  $Ce^{4+}$  over  $Ce^{3+}$ , both of which occur in siliceous melts in relative proportions that depend on the melt oxidation state (Hinton and Upton, 1991). As  $Ce^{4+}$  exchanges directly for  $Zr^{4+}$ , its partitioning will be independent of H and contents, in contrast to  $Ce^{3+}$ . Thus, Ce anomalies will be different for zircons from melts with identical oxidation states but different H or P contents. For instance, using the

equilibrium partitioning model, increasing both H and P in the melt by a factor two would result in an increase in La and Pr in zircon by a factor two. In contrast, the increase in Ce would be negligible as it is dominated by  $Ce^{4+}$ , which is not dependent on H or P contents. In a zircon with  $Ce/Ce^* = 20$  initially,  $Ce/Ce^*$  would therefore decrease to 10.5, equivalent to a decrease in apparent  $f_{O_2}$  by 2.5 log units according to the model by Trail et al. (2012). This is similar to experimental observations by Burnham and Berry (2012), who noticed that in experiments with high oxidation states and therefore high  $Ce^{4+}$  activity, Ce differed little between different sectors, whereas all other REE were clearly affected. This limits the applicability of experimental Ce partitioning data for estimating melt oxidation state (Burnham and Berry, 2012; Trail et al., 2012) to systems with broadly similar H and P contents. In contrast, Eu anomalies are probably not affected, as in zircon it is a reflection of the Eu anomaly of the melt and not a result of preferential incorporation of one of the species into zircon (Hoskin and Schaltegger, 2003) and  $Eu^{2+}$  and  $Eu^{3+}$  are likely to be similarly affected by charge balance effects on trace element partitioning.

It is worth noting that Eq. (4) does not apply to water incorporated in zircon by other substitution mechanisms. For example, the average  $H_2O$  solubility in zircon is found to be 188 ppmw in undoped zircons (Trail et al., 2011), which is the result of hydrogrossular substitution. Potentially, H in zircon may be used to constrain water contents in REE-poor melts with low silica activities, but this will need additional experimental confirmation. However,  $H_2O$  contents of REE-bearing siliceous melts cannot be accurately reconstructed from H in zircon without knowledge of P and REE contents of the melt. Further work is needed to constrain the interdependent partition coefficients of H, P and REE between zircon and melt.

## 5. CONCLUSIONS

- (a) Water contents as measured by SIMS in zircons from Fe-Ti gabbros from the Vema Lithospheric Section (Mid-Atlantic Ridge) range from <15 to 1212 ppmw and correlate strongly with REE and P contents. FTIR absorption spectra of these zircons are very similar to those of experimentally grown Lu-doped hydrous zircons, showing a main absorption band at  $3100\text{ cm}^{-1}$ .
- (b) Water is incorporated following the nominal reaction  $H^+ + REE^{3+} = Zr^{4+}$  and therefore competes with P for REE, as P is incorporated following the xenotime reaction:  $P^{5+} + REE^{3+} = Zr^{4+} + Si^{4+}$ . Other trace elements are too low in concentration to play a role in the charge balance.
- (c) Equilibrium partitioning of charge-coupled trace elements depends on the activity in the melt of all elements taking part in the exchange reaction. Thus water uptake in zircon depends on not only on H but also P and REE contents of the melt. This makes estimating water contents in the melt from H in zircon very challenging.

- (d) Most zircons show sector zoning. The fastest growing sector is enriched in P but depleted in H and REE compared to the slower growing sector. As P is depleted in zircon relative to the melt and REE are enriched, this suggests that diffusion to (for REE) and from (for P) the boundary layer limits the uptake of these elements in zircon.
- (e) REE partitioning in zircon is dependent on H and P contents of the melt. As Ce in zircon occurs primarily as Ce<sup>4+</sup> and therefore exchanges directly for Zr (and is independent of P and H in the melt), Ce anomalies (Ce/ $\sqrt{(\text{La} \times \text{Pr})}$ ) are dependent on H and P in the melt. This should be taken into account when modeling magma oxidation state based on Ce anomalies.

#### ACKNOWLEDGEMENTS

We thank Enrico Bonatti, Daniele Brunelli and the IFREMER Lithothèque for providing samples. Laurence Coogan and Jon Blundy are thanked for discussions about REE partitioning into zircon and Nicola Cayzer for EBSD analysis and interpretation. Jed Mosenfelder and an anonymous reviewer are thanked for constructive comments and Anders Meibom for editorial handling.

This work was supported by the Natural Environment Research Council (NERC Grant reference number NE/H020004/1 to Lissenberg), and Ion Microprobe Facility Grant IMF441/1011 (Lissenberg). D.T. thanks the NASA Astrobiology Institute Grant no. NNA09DA80A to RPI for support. R.B. was funded by ERC Advanced Grant "CRITMAG".

#### APPENDIX A. SUPPLEMENTARY DATA

Supplementary data associated with this article can be found, in the online version, at <http://dx.doi.org/10.1016/j.gca.2014.06.033>.

#### REFERENCES

- Aines R. D. and Rossman G. R. (1986) Relationships between radiation-damage and trace water in zircon, quartz, and topaz. *Am. Mineral.* **71**, 1186–1193.
- Auzende J. M., Bideau D., Bonatti E., Cannat M., Honnorez J., Lagabrielle Y., Malavieille J., Mamaloukasfrangoulis V. and Mevel C. (1988) A complete section of the oceanic crust on the southern wall of the Vema fracture zone, central Atlantic: preliminary results of the Vemanaute cruise. *C. R. Acad. Sci. Ser. II* **307**, 2061–2067.
- Auzende J. M., Bideau D., Bonatti E., Cannat M., Honnorez J., Lagabrielle Y., Malavieille J., Mamaloukasfrangoulis V. and Mevel C. (1989) Direct observation of a section through slow-spreading oceanic-crust. *Nature* **337**, 726–729.
- Bell D. R., Rossman G. R. and Moore R. O. (2004) Abundance and partitioning of OH in a high-pressure magmatic system: megacrysts from the Monastery kimberlite, South Africa. *J. Petrol.* **45**, 1539–1564.
- Belousova E. A., Griffin W. L., O'Reilly S. Y. and Fisher N. I. (2002) Igneous zircon: trace element composition as an indicator of source rock type. *Contrib. Mineral. Petrol.* **143**, 602–622.
- Berry A. J., Hermann J., O'Neill H. S. C. and Foran G. J. (2005) Fingerprinting the water site in mantle olivine. *Geology* **33**, 869–872.
- Blundy J., Cashman K. V. and Berlo K. (2008) Evolving magma storage conditions beneath Mount St. Helens inferred from chemical variations in melt inclusions from the 1980–1986 and current (2004–2006) eruptions. In *A Volcano Rekindled; The Renewed Eruption of Mount St. Helens, 2004–2006* (eds. D. R. Sherrod, W.E. Scott and P.H. Stauffer), p. 1750.
- Bonatti E., Ligi M., Brunelli D., Cipriani A., Fabretti P., Ferrante V., Gasperini L. and Ottolini L. (2003) Mantle thermal pulses below the Mid-Atlantic Ridge and temporal variations in the formation of oceanic lithosphere. *Nature* **423**, 499–505.
- Bonatti E., Brunelli D., Buck W. R., Cipriani A., Fabretti P., Ferrante V., Gasperini L. and Ligi M. (2005) Flexural uplift of a lithospheric slab near the Vema transform (Central Atlantic): timing and mechanisms. *Earth Planet. Sci. Lett.* **240**, 642–655.
- Botis S. M., Pan Y. M. and Ewing R. C. (2013) Hydrogen incorporation in crystalline zircon: insight from ab initio calculations. *Am. Mineral.* **98**, 745–751.
- Brunelli D., Seyler M., Cipriani A., Ottolini L. and Bonatti E. (2006) Discontinuous melt extraction and weak refertilization of mantle peridotites at the Vema lithospheric section (Mid-Atlantic Ridge). *J. Petrol.* **47**, 745–771.
- Burnham A. D. and Berry A. J. (2012) An experimental study of trace element partitioning between zircon and melt as a function of oxygen fugacity. *Geochim. Cosmochim. Acta* **95**, 196–212.
- Cavosie A. J., Valley J. W. and Wilde S. A. (2005) Magmatic delta O-18 in 4400–3900 Ma detrital zircons: a record of the alteration and recycling of crust in the Early Archean. *Earth Planet. Sci. Lett.* **235**, 663–681.
- Cavosie A. J., Kita N. T. and Valley J. W. (2009) Primitive oxygen-isotope ratio recorded in magmatic zircon from the Mid-Atlantic Ridge. *Am. Mineral.* **94**, 926–934.
- Cavosie A. J., Valley J. W., Kita N. T., Spicuzza M. J., Ushikubo T. and Wilde S. A. (2011) The origin of high delta O-18 zircons: marbles, megacrysts, and metamorphism. *Contrib. Mineral. Petrol.* **162**, 961–974.
- Cliff J., Pidgeon B. and Nemchin A. (2013) <sup>16</sup>O<sup>1</sup>H Signal as an indication of metamict O-contamination in zircon (abstract). *Mineral. Mag.* **77**, 897.
- Coleman R.G. and Erd R.C. (1961). Hydrozircon from the wind river formation, Wyoming. *U.S. Geological Survey Professional Paper* 424-C, pp. 297–300.
- De Hoog J. C. M., Taylor B. E. and Van Bergen M. J. (2009) Hydrogen-isotope systematics in degassing basaltic magma and application to Indonesian arc basalts. *Chem. Geol.* **266**, 265–275.
- Dowty E. (1976) Crystal-structure and crystal-growth. 2. Sector zoning in minerals. *Am. Mineral.* **61**, 460–469.
- Ferry J. M. and Watson E. B. (2007) New thermodynamic models and revised calibrations for the Ti-in-zircon and Zr-in-rutile thermometers. *Contrib. Mineral. Petrol.* **154**, 429–437.
- Finch R. J., Hanchar J. M., Hoskin P. W. O. and Burns P. C. (2001) Rare-earth elements in synthetic zircon: Part 2. A single-crystal X-ray study of xenotime substitution. *Am. Mineral.* **86**, 681–689.
- Fowler A., Prokoph A., Stern R. and Dupuis C. (2002) Organization of oscillatory zoning in zircon: analysis, scaling, geochemistry, and model of a zircon from Kipawa, Quebec, Canada. *Geochim. Cosmochim. Acta* **66**, 311–328.
- Frondel C. (1953) Hydroxyl substitution in thorite and zircon. *Am. Mineral.* **38**, 1007–1018.
- Grimes C. B., John B. E., Cheadle M. J., Mazdab F. K., Wooden J. L., Swapp S. and Schwartz J. J. (2009) On the occurrence, trace element geochemistry, and crystallization history of zircon from in situ ocean lithosphere. *Contrib. Mineral. Petrol.* **158**, 757–783.

- Hanchar J. M. and van Westrenen W. (2007) Rare earth element behavior in zircon-melt systems. *Elements* **3**, 37–42.
- Hanchar J. M., Finch R. J., Hoskin P. W. O., Watson E. B., Cherniak D. J. and Mariano A. N. (2001) Rare earth elements in synthetic zircon: Part I. Synthesis, and rare earth element and phosphorus doping. *Am. Mineral.* **86**, 667–680.
- Harrison T. M. and Watson E. B. (1984) The behavior of apatite during crustal anatexis – equilibrium and kinetic considerations. *Geochim. Cosmochim. Acta* **48**, 1467–1477.
- Harrison T. M., Schmitt A. K., McCulloch M. T. and Lovera O. M. (2008) Early ( $\geq 4.5$  Ga) formation of terrestrial crust: Lu–Hf, delta O-18, and Ti thermometry results for Hadean zircons. *Earth Planet. Sci. Lett.* **268**, 476–486.
- Hinton R. W. and Upton B. G. J. (1991) The chemistry of zircon – variations within and between large crystals from syenite and alkali basalt xenoliths. *Geochim. Cosmochim. Acta* **55**, 3287–3302.
- Hinton R., Macdonald R., MacGarvie D., Tindle A. and Harley S. (2003) *The Possible Role of Hydrogen in the Substitution of Rare Earth Elements into Zircon* (abstract). EGS-AGU-EUG Joint Assembly, European Geophysical Society, Nice, France, p. 05968.
- Hoskin P. W. O. (2000) Patterns of chaos: fractal statistics and the oscillatory chemistry of zircon. *Geochim. Cosmochim. Acta* **64**, 1905–1923.
- Hoskin P. W. O. and Schaltegger U. (2003) The composition of zircon and igneous and metamorphic petrogenesis. *Zircon* **53**, 27–62.
- Ihinger P. D., Zhang Y. X. and Stolper E. M. (1999) The speciation of dissolved water in rhyolitic melt. *Geochim. Cosmochim. Acta* **63**, 3567–3578.
- Jacobsen S. D. (2006) Effect of water on the equation of state of nominally anhydrous minerals. *Rev. Mineral. Geochem.* **62**, 321–342.
- Jochum K. P., Weis U., Stoll B., Kuzmin D., Yang Q. C., Raczek I., Jacob D. E., Stracke A., Birbaum K., Frick D. A., Gunther D. and Enzweiler J. (2011) Determination of reference values for NIST SRM 610–617 glasses following ISO guidelines. *Geostand. Geoanal. Res.* **35**, 397–429.
- Kohlstedt D. L. (2006) The role of water in high-temperature rock deformation. *Rev. Mineral. Geochem.* **62**, 377–396.
- Kohn S. C. and Grant K. J. (2006) The partitioning of water between nominally anhydrous minerals and silicate melts. *Rev. Mineral. Geochem.* **62**, 231–241.
- Lissenberg C. J., Rioux M., Shimizu N., Bowring S. A. and Mevel C. (2009) Zircon dating of oceanic crustal accretion. *Science* **323**, 1048–1050.
- Maas R., Kinny P. D., Williams I. S., Froude D. O. and Compston W. (1992) The Earth's oldest known crust – a geochronological and geochemical study of 3900–4200 Ma old detrital zircons from Mt Narryer and Jack Hills, Western-Australia. *Geochim. Cosmochim. Acta* **56**, 1281–1300.
- Mangan M. and Sisson T. (2000) Delayed, disequilibrium degassing in rhyolite magma: decompression experiments and implications for explosive volcanism. *Earth Planet. Sci. Lett.* **183**, 441–455.
- Murakami T., Chakoumakos B. C., Ewing R. C., Lumpkin G. R. and Weber W. J. (1991) Alpha-decay event damage in zircon. *Am. Mineral.* **76**, 1510–1532.
- Nasdala L., Beran A., Libowitzky E. and Wolf D. (2001) The incorporation of hydroxyl groups and molecular water in natural zircon (ZrSiO<sub>4</sub>). *Am. J. Sci.* **301**, 831–857.
- Ohtani E. and Litasov K. D. (2006) The effect of water on mantle phase transitions. *Rev. Mineral. Geochem.* **62**, 397–420.
- Ottolini L., Camara F., Hawthorne F. C. and Stirling J. (2002) SIMS matrix effects in the analysis of light elements in silicate minerals: comparison with SREF and EMPA data. *Am. Mineral.* **87**, 1477–1485.
- Regenauer-Lieb K. (2006) Water and geodynamics. *Rev. Mineral. Geochem.* **62**, 451–473.
- Smyth J. R. (1987) Beta-Mg<sub>2</sub>SiO<sub>4</sub> – a potential host for water in the mantle. *Am. Mineral.* **72**, 1051–1055.
- Smyth J. R. (2006) Hydrogen in high pressure silicate and oxide mineral structures. *Rev. Mineral. Geochem.* **62**, 85–115.
- Speer J. A. (1980) Zircon In *Orthosilicates* (First ed.) (ed. P. H. Ribbe), *Reviews in Mineralogy* **5**, pp. 67–112.
- Stolper E. (1982) The speciation of water in silicate melts. *Geochim. Cosmochim. Acta* **46**, 2609–2620.
- Trail D., Mojzsis S. J., Harrison T. M., Schmitt A. K., Watson E. B. and Young E. D. (2007) Constraints on Hadean zircon protoliths from oxygen isotopes, Ti-thermometry, and rare earth elements. *Geochim. Geophys. Geosyst.* **8**.
- Trail D., Thomas J. B. and Watson E. B. (2011) The incorporation of hydroxyl into zircon. *Am. Mineral.* **96**, 60–67.
- Trail D., Watson E. B. and Tailby N. D. (2012) Ce and Eu anomalies in zircon as proxies for the oxidation state of magmas. *Geochim. Cosmochim. Acta* **97**, 70–87.
- Ushikubo T., Kita N. T., Cavosie A. J., Wilde S. A., Rudnick R. L. and Valley J. W. (2008) Lithium in Jack Hills zircons: evidence for extensive weathering of Earth's earliest crust. *Earth Planet. Sci. Lett.* **272**, 666–676.
- Watson E. B. and Liang Y. (1995) A simple model for sector zoning in slowly grown crystals: implications for growth rate and lattice diffusion, with emphasis on accessory minerals in crustal rocks. *Am. Mineral.* **80**, 1179–1187.
- Wiedenbeck M., Hanchar J. M., Peck W. H., Sylvester P., Valley J., Whitehouse M., Kronz A., Morishita Y., Nasdala L., Fiebig J., Franchi I., Girard J. P., Greenwood R. C., Hinton R., Kita N., Mason P. R. D., Norman M., Ogasawara M., Piccoli R., Rhede D., Satoh H., Schulz-Dobrick B., Skar O., Spicuzza M. J., Terada K., Tindle A., Togashi S., Vennemann T., Xie Q. and Zheng Y. F. (2004) Further characterisation of the 91500 zircon crystal. *Geostand. Geoanal. Res.* **28**, 9–39.
- Wilde S. A., Valley J. W., Peck W. H. and Graham C. M. (2001) Evidence from detrital zircons for the existence of continental crust and oceans on the Earth 4.4 Gyr ago. *Nature* **409**, 175–178.
- Wood B. J. and Blundy J. D. (2001) The effect of cation charge on crystal-melt partitioning of trace elements. *Earth Planet. Sci. Lett.* **188**, 59–71.
- Woodhead J. A., Rossman G. R. and Silver L. T. (1991a) The metamictization of zircon – radiation dose-dependent structural characteristics. *Am. Mineral.* **76**, 74–82.
- Woodhead J. A., Rossman G. R. and Thomas A. P. (1991b) Hydrous species in zircon. *Am. Mineral.* **76**, 1533–1546.
- Zhang Y. X. (1999) H<sub>2</sub>O in rhyolitic glasses and melts: measurement, speciation, solubility, and diffusion. *Rev. Geophys.* **37**, 493–516.
- Zhang M., Salje E. K. H. and Ewing R. C. (2002) Infrared spectra of Si–O overtones, hydrous species, and U ions in metamict zircon: radiation damage and recrystallization. *J. Phys. Condens. Matter* **14**, 3333–3352.